*11514–11526* *Nucleic Acids Research, 2019, Vol. 47, No. 22* *Published online 14 November 2019*
*doi: 10.1093/nar/gkz987*

# Sulfur-centered hemi-bond radicals as active intermediates in S-DNA phosphorothioate oxidation

**Jialong Jie[1], Ye Xia[1], Chun-Hua Huang[2], Hongmei Zhao[3], Chunfan Yang[1], Kunhui Liu[1], Di Song[3], Ben-Zhan Zhu[2] and Hongmei Su[1,*]**

[1]College of Chemistry, Beijing Normal University, Beijing 100875, China, [2]State Key Lab of Environmental Chemistry and Ecotoxicology, Research Center for Eco-Environmental Science, Chinese Academy of Sciences, Beijing 100085, China and [3]Beijing National Laboratory for Molecular Sciences (BNLMS), Institute of Chemistry, Chinese Academy of Sciences, Beijing 100190, China

Received August 21, 2019; Revised October 10, 2019; Editorial Decision October 11, 2019; Accepted October 18, 2019

## ABSTRACT

**Phosphorothioate (PS) modifications naturally appear in bacteria and archaea genome and are widely used as antisense strategy in gene therapy. But the chemical effects of PS introduction as a redox active site into DNA (S-DNA) is still poorly understood. Herein, we perform time-resolved spectroscopy to examine the underlying mechanisms and dynamics of the PS oxidation by potent radicals in free model, in dinucleotide, and in S-oligomer. The crucial sulphur-centered hemi-bonded intermediates -P–S.·.S–P- were observed and found to play critical roles leading to the stable adducts of -P–S–S–P-, which are backbone DNA lesion products. Moreover, the oxidation of the PS moiety in dinucleotides d[$G_{PS}$G], d[$A_{PS}$A], d[$G_{PS}$A], d[$A_{PS}$G] and in S-oligomers was monitored in real-time, showing that PS oxidation can compete with adenine but not with guanine. Significantly, hole transfer process from $A^{+\bullet}$ to PS and concomitant -P–S.·.S–P- formation was observed, demonstrating the base-to-backbone hole transfer unique to S-DNA, which is different from the normally adopted backbone-to-base hole transfer in native DNA. These findings reveal the distinct backbone lesion pathway brought by the PS modification and also imply an alternative -P–S.·.S–P-/-P–S–S–P- pathway accounting for the interesting protective role of PS as an oxidation sacrifice in bacterial genome.**

## INTRODUCTION

Development of antisense technology is a conceptually simple process that involves designing an appropriately modified complementary oligonucleotide based on the sequence of the targeted messenger ribonucleic acid. Phosphorothioate (PS) oligonucleotides in which one of the nonbridging phosphate oxygens is replaced by sulfur are one of the most popular oligonucleotide modifications due to their advantageous pharmacokinetic properties, bioavailability, and the nuclease resistance *in vivo* (Figure 1A) (1–4). The S-DNA oligomer has shown great potential in different therapeutic areas for the treatment of cancer (5–7), Alzheimer's disease (8), rheumatoid arthritis (9) and different kinds of viral infections (10).

Importantly, recent studies showed that the PS modification can naturally appear in bacteria and archaea genome, which plays protective roles against internucleotide bond cleavage (11). Additionally, it was proposed that PS can play an antioxidant role in the hosting bacteria against peroxide (12), and later a desulphurization process induced by hydroxyl radical under the negative electrospray ionization mass spectroscopy conditions was noticed (13). Although its great potential for general oligonucleotide therapeutic applications and biological significance have been gradually recognized, the chemical stability and reactivity of the S-DNA oligomer is still poorly understood, and this topic is of great interest in biomedical and biochemical research. The chemical modification with PS causes minimal perturbation of DNA conformation and base stacking (14,15), but the ionization potential of the PS moiety is expected to be lower than those of the phosphate moiety (16). Under the attack of potent oxidant radicals, the PS moiety in an S-DNA oligomer should serve as an additional redox active site, and it may compete with the oxidation of guanine (G) and adenine (A), leading to a variety of lesion products (17–21) or acting as oxidation sacrifice to protect genes (12).

In sulfur chemistry and biochemistry, S.·.X hemi-bond radical formation (Figure 1B) due to the interaction between a singly occupied lone pair orbital of sulfur and a doubly occupied $\pi$ or lone pair orbital of X is found to play critical roles, particularly in oxidation reactions involving sulfur radical cations. For example, the S.·.$\pi$ hemi bond

*To whom correspondence should be addressed. Tel: +86 10 5880 7159; Email: hongmei@bnu.edu.cn

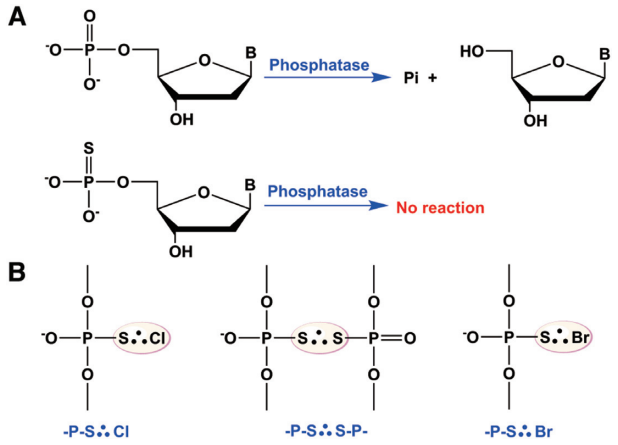


**Figure 1.** (**A**) Scheme showing the resistance of nucleoside 5′-phosphorothioate against alkaline phosphatase. (**B**) Schematic structures of the hemi-bonded species -P–S.·.Cl, -P–S.·.S–P- and -P- S.·.Br.

between a sulfur-containing residue and a phenyl ring in the oxidation of protein can serve as a potent relay station in multistep electron hopping processes (22–24). The rich S.·.S, S.·.π and S–π–S hemi-bond motifs in the simplest model systems containing $(H_2S)^+$ radical cation clusters have been recently identified and characterized in the gas phase (25–27). Interestingly, two hemi-bonded species, -P–S.·.Cl and -P–S.·.S–P-, were detected in the oxidation of PS-containing dsDNA oligomers (S-oligomers) by $Cl_2^{-\bullet}$ using steady-state electron spin resonance (ESR) at low temperatures (16). Thus, the oxidation of the PS moiety in S-DNA by an oxidizing radical may not be simply a direct one-electron oxidation process but that it most likely follows intricate mechanisms involving sulfur-centered intermediates with hemi-bonded structures. However, time-resolved spectroscopic identification and characterization of such transient intermediates remain elusive, and this knowledge is crucial for revealing the molecular elementary mechanisms and dynamics of S-DNA oxidation. Virtually, hemi-bonded structures are one of the fundamental bonding phenomena in chemistry and biology and have attracted great interests (16,23,25,28–39).

Herein, we perform systematic transient UV–Vis spectroscopy study to capture the intermediates and track the reaction dynamics in real-time. Specifically, for the oxidation of PS in the free model, two kinds of hemi-bonded intermediates, -P–S.·.S–P- (410 nm) and -P–S.·.Br (380 nm), are observed in the transient spectra. The unique spectral signatures with a large oscillator strength ($\sigma\sigma^*$) associated with these hemi-bonded species have been identified and well rationalized by time-dependent DFT (TD-DFT) calculations. Together with kinetics analysis, complementary HPLC and MS measurements present evidence that the decay of -P–S.·.S–P- can result in the formation of -P–S–S–P- adducts, which is a type of DNA backbone lesion, or serve as an alternative pathway to protect against the damage of base. The PS oxidation rate constants were measured and found to be comparable to those of the oxidation of G and A. Importantly, the oxidation process of PS in competition with G and A in dinucleotides and S-DNA oligomers was monitored in real-time, revealing direct hole transfer from $A^{+\bullet}$/A(-H)$^\bullet$ to PS and concomitant -P–S.·.S–P- formation. The redox active property of PS is found to result in base-to-backbone hole transfer (with rates of $10^4$ $s^{-1}$) and the ensuing backbone lesions, which is unique to S-DNA.

## MATERIALS AND METHODS

### Materials

Sodium persulfate ($Na_2S_2O_8$, Sigma-Aldrich), Lithium chloride (LiCl, Aladdin), Lithium bromide (LiBr, Aladdin), Hydrogen peroxide ($H_2O_2$, 15%, Beijing ShiJi), and O,O-Diethyl thiophosphate potassium salt($C_4H_{10}KPSO_3$, Sigma-Aldrich) were used without further purification. Dinucleotides (*d*[GG], *d*[AA]), PS-containing dinucleotides (*d*[$G_{PS}$G], *d*[$A_{PS}$A]) and PS-containing oligonucleotides (($A_{PS}$ATT)$_3$, (AAT$_{PS}$T)$_3$, ($A_{PS}$ATC)$_3$, and (AAT$_{PS}$C)$_3$) (PS indicates the phophorus–sulfur bond) were purchased from Sangon Biotech (Shanghai) Co., Ltd in the polyacrylamide gel electrophoresis-purified form.

The concentrations of dinucleotides, PS-containing dinucleotides, and PS-containing oligonucleotides were determined by monitoring the absorbance at 260 nm in the UV–Vis spectra and using the corresponding extinction coefficients of 21 600 $M^{-1}$ $cm^{-1}$ for *d*[GG] and *d*[$G_{PS}$G], 27 400 $M^{-1}$ $cm^{-1}$ for *d*[AA] and *d*[$A_{PS}$A], 127 300 $M^{-1}$ $cm^{-1}$ for ($A_{PS}$ATT)$_3$ and (AAT$_{PS}$T)$_3$ and 123 700 $M^{-1}$ $cm^{-1}$ for ($A_{PS}$ATC)$_3$ and (AAT$_{PS}$C)$_3$, respectively. Ultrapure water obtained by Millipore filtration was used as solvent.

### Laser flash photolysis

Nanosecond time-resolved transient absorption spectra were measured using a flash photolysis setup Edinburgh LP920 spectrometer (Edinburgh Instruments Ltd) combined with a Nd:YAG laser (Spectra-Physics Lab 170, Newport Corp.). Each measurement was performed in a 1 cm path length quartz cuvette at room temperature. The sample was excited by a 355 nm laser pulse (1 Hz, 20 mJ/pulse/$cm^2$, fwhm ≈ 7 ns). The analyzing light was from a 450 W pulsed xenon lamp. A monochromator equipped with a photomultiplier for collecting the spectral range from 300 to 700 nm was used to analyze transient absorption spectra. The signals from the photomultiplier were displayed and recorded as a function of time on a 100 MHz (1.25 Gs/s sampling rate) oscilloscope (Tektronix, TDS 3012C), and the data were transferred to a personal computer. Data were analyzed by the online software of the LP920 spectrophotometer. The fitting quality was judged by weighted residuals and reduced $\chi^2$ value.

### HPLC–ESI-Q-TOF-MS

The samples were analyzed by HPLC coupled with ESI-Q-TOF-MS(Agilent 6540). The separation column was EclipsePlus C18 column (2.1 × 100 mm, 1.8 μm) from Agilent. Optimum separation was achieved with a binary mobile phase (deionized water:$CH_3CN$ = 20:80 in volume) with a flow rate at 0.2 ml/min. Capillary and fragmentor voltages were 2500 and 75 V respectively; desolvation temperature was 300°C. Nitrogen was used as the drying gas.

The collision gas was argon at the pressure of $5.0 \times 10^{-5}$ Torr (1 Torr = 133.322 Pa), and the collision energy was 10 V. The pressure in the TOF region was lower than $3.0 \times 10^{-7}$ Torr.

### Calculation methods

The geometry was fully optimized at the CAM-B3LYP/6–311++G(3df,3pd) level of theory. The vertical excited state UV–vis spectrum was calculated using time-dependent (TD) CAM-B3LYP method based on the geometry optimized at the same level. Bulk solvation effects were simulated by using the polarizable continuum model (PCM). We used (TD) CAM-B3LYP method for geometry optimization and excited state calculations because this functional is appropriate for long range interaction involving charge transfer excited states (40). The CAM-B3LYP method is a long-range corrected hybrid functional and found to be very successful to study the excited state of systems involving charge transfer states (41).

All the calculations were carried out using the Gaussian 09 program package (42). GaussView molecular modeling software was used to plot the molecular orbitals and draw the molecular structure. For these particular computations, the ethyl group was replaced with a methyl group in order to reduce the computational load.

## RESULTS

### Oxidation of PS by $Cl_2^{-\bullet}$, $Br_2^{-\bullet}$, $SO_4^{-\bullet}$ and $OH^\bullet$ radicals

$$S_2O_8^{2-} \xrightarrow{hv} 2SO_4^{-\bullet} \quad (1)$$

$$SO_4^{-\bullet} + 2Cl^- \rightarrow SO_4^{2-} + Cl_2^{-\bullet} \quad (2)$$

$$SO_4^{-\bullet} + 2Br^- \rightarrow SO_4^{2-} + Br_2^{-\bullet} \quad (3)$$

$$H_2O_2 \xrightarrow{hv} 2OH^\bullet \quad (4)$$

Sulfate radicals ($SO_4^{-\bullet}$) were generated by the photodissociation of peroxodisulfate anions ($S_2O_8^{2-}$) induced by nanosecond 355 nm laser pulse (Equation 1) (43–45). The photodissociation of $S_2O_8^{2-}$ is rapid, and all $SO_4^{-\bullet}$ radicals are generated within the ~14 ns laser pulse duration. If excess $Cl^-$ or $Br^-$ is present, then the $SO_4^{-\bullet}$ radicals are converted into $Cl_2^{-\bullet}$ or $Br_2^{-\bullet}$ radicals, a rapid reaction that is also complete within the laser pulse duration (Equations 2 and 3) (46–48). Indeed, it is seen in Figure 2A and B that the transient absorption bands of $Cl_2^{-\bullet}$ ($\lambda_{max}$ = 340 nm) (49) and $Br_2^{-\bullet}$ ($\lambda_{max}$ = 360 nm) (46,50) reach their maximum intensity within 20 ns after the laser pulse. Hydroxyl radicals ($OH^\bullet$) were generated by the photodissociation of hydrogen peroxide ($H_2O_2$, 15%) (51). The photodissociation of $H_2O_2$ is rapid, and all $OH^\bullet$ radicals are expected to be generated within the laser pulse duration (Equation 4). The photolysis of the $H_2O_2$ solution alone provides a blank background in the transient UV–vis spectra.

The instantaneous formation of these radicals within the laser pulse ensures no interference with the detection of the subsequent oxidation reaction with PS. Also, the PS or S-DNA oligomer does not absorb 355 nm and the photolysis of PS or S-DNA oligomer alone does not generate any signal, providing a neat background.

The successive radical oxidation reaction of PS in the free model (*O*,*O*-diethyl thiophosphate) was first monitored in the presence of $Cl_2^{-\bullet}$ radicals (Figure 2C). Due to the efficient reaction with PS, the decay of the $Cl_2^{-\bullet}$ band at 340 nm is accelerated, which is accompanied by the buildup of a transient feature with a strong peak at 410 nm within 1 μs (Figure 2C, E). This result indicates that the peak at 410 nm signifies a new species corresponding to $Cl_2^{-\bullet}$ + PS and its subsequent reaction. According to previous ESR studies of the PS + $Cl_2^{-\bullet}$ reaction (16), the electrophilic addition of $Cl_2^{-\bullet}$ to PS with the elimination of $Cl^-$ leads to the formation of the hemi-bonded adduct intermediate -P–S.·.Cl, and this intermediate further reacts with a neighboring PS to form another hemi-bonded intermediate (-P–S.·.S–P-). Is the transient feature at 410 nm ascribed to one of the hemi-bonded species, -P–S.·.Cl or -P–S.·.S–P-? Considering that the spectral signature of -P–S.·.Cl should be related to the oxidant radicals ($Cl_2^{-\bullet}$), while that of -P–S.·.S–P- is not, the assignment of the new transient species can be assisted by changing the oxidant radicals.

We then performed control experiments for the oxidation of PS by $SO_4^{-\bullet}$ or $OH^\bullet$. The transient spectra obtained after a 200 ns delay for the PS + $SO_4^{-\bullet}$ reaction are identical to those for the PS + $Cl_2^{-\bullet}$ reaction (Supplementary Figure S1), and the strong absorption band at 410 nm in both reactions decay identically (Supplementary Figure S2). In addition, the features of the transient absorption spectra for PS + $OH^\bullet$ (Supplementary Figure S3) are also the same as those observed for the PS + $Cl_2^{-\bullet}$ and PS + $SO_4^{-\bullet}$ reactions. Thus, the absorption bands at 410 nm that are observed in all three reactions, PS + $Cl_2^{-\bullet}$, PS + $SO_4^{-\bullet}$ and PS + $OH^\bullet$, are seemingly unrelated to the oxidant radicals and thus should be most likely ascribed to the same species, namely, -P–S.·.S–P-.

For PS oxidation by $Cl_2^{-\bullet}$, the transient species -P–S.·.S–P- could be formed through the reaction between the hemi-bonded intermediate -P–S.·.Cl and a second PS (Figure 3A) (16). Nevertheless, as shown in Figure 3A, another pathway for the one-electron oxidation of PS to a radical cation (-P–$S^{+\bullet}$) that complexes with a second PS resulting in -P–S.·.S–P- should be most likely involved, especially for $SO_4^{-\bullet}$ and $OH^\bullet$, which are stronger oxidant radicals (52) than $Cl_2^{-\bullet}$. Actually, the oxidation of some thioethers and β-hydroxysulfides with strong oxidant radicals, e.g. $OH^\bullet$, provides evidence that these reactions can proceed via electron abstraction from sulfur to give monomeric radical cations (29,53–55). For example, the oxidation of dimethyl sulfide ($Me_2S$) gives an ESR signal assigned to $[Me_2S.\cdot.Me_2S]^+$ that is formed from the intermediate radical cation $Me_2S^{+\bullet}$ by reaction with a second $Me_2S$ (29). Regardless of the underlying oxidation pathways, the evidence that the decay dynamics of $Cl_2^{-\bullet}$ (340 nm) is concomitant with the generation of -P–S.·.S–P- (410 nm) (Figure 2C, E) indicates that the oxidation of PS by $Cl_2^{-\bullet}$ should be the rate-determining step in the consecutive reaction to form -P–S.·.S–P- (Figure

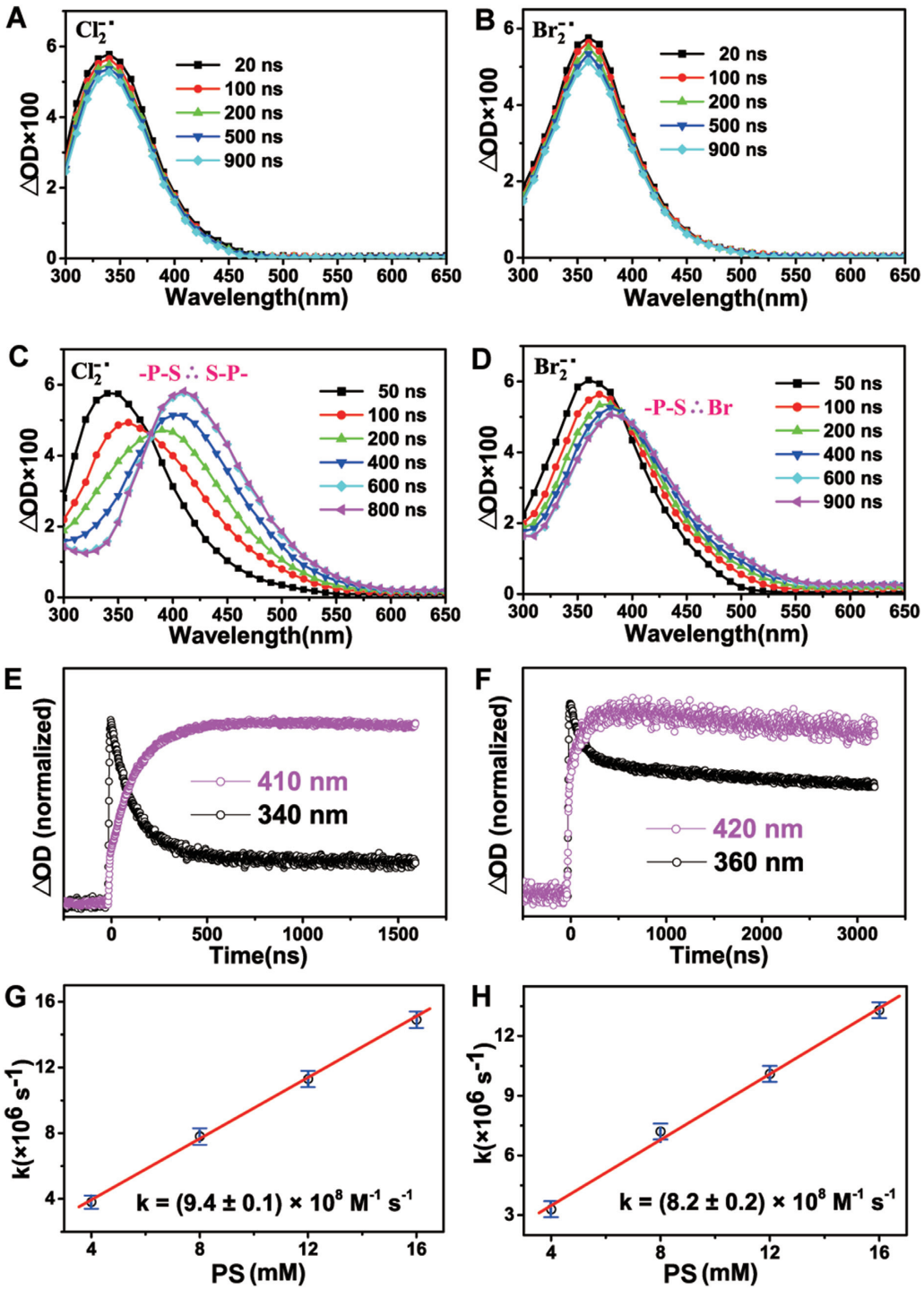


**Figure 2.** Transient absorption spectra obtained after 355 nm laser flash photolysis of (**A**) $Na_2S_2O_8$ + LiCl, (**B**) $Na_2S_2O_8$ + LiBr, (**C**) $Na_2S_2O_8$ + LiCl + PS and (**D**) $Na_2S_2O_8$ + LiBr + PS. (**E**) Normalized absorption changes at 340 and 410 nm after laser flash photolysis of $Na_2S_2O_8$ + LiCl + PS. (**F**) Normalized absorption changes at 360 and 420 nm after laser flash photolysis of $Na_2S_2O_8$ + LiBr + PS. The concentration of $Na_2S_2O_8$, LiCl, LiBr, and PS used in above experiments is 300 mM, 1.0 M, 1.0 M and 8 mM, respectively. Concentration dependence of rate constants obtained from the decay of (**G**) 340 nm for $Cl_2^{-\bullet}$ and (**H**) 360 nm for $Br_2^{-\bullet}$ (the red line is the fitted line).

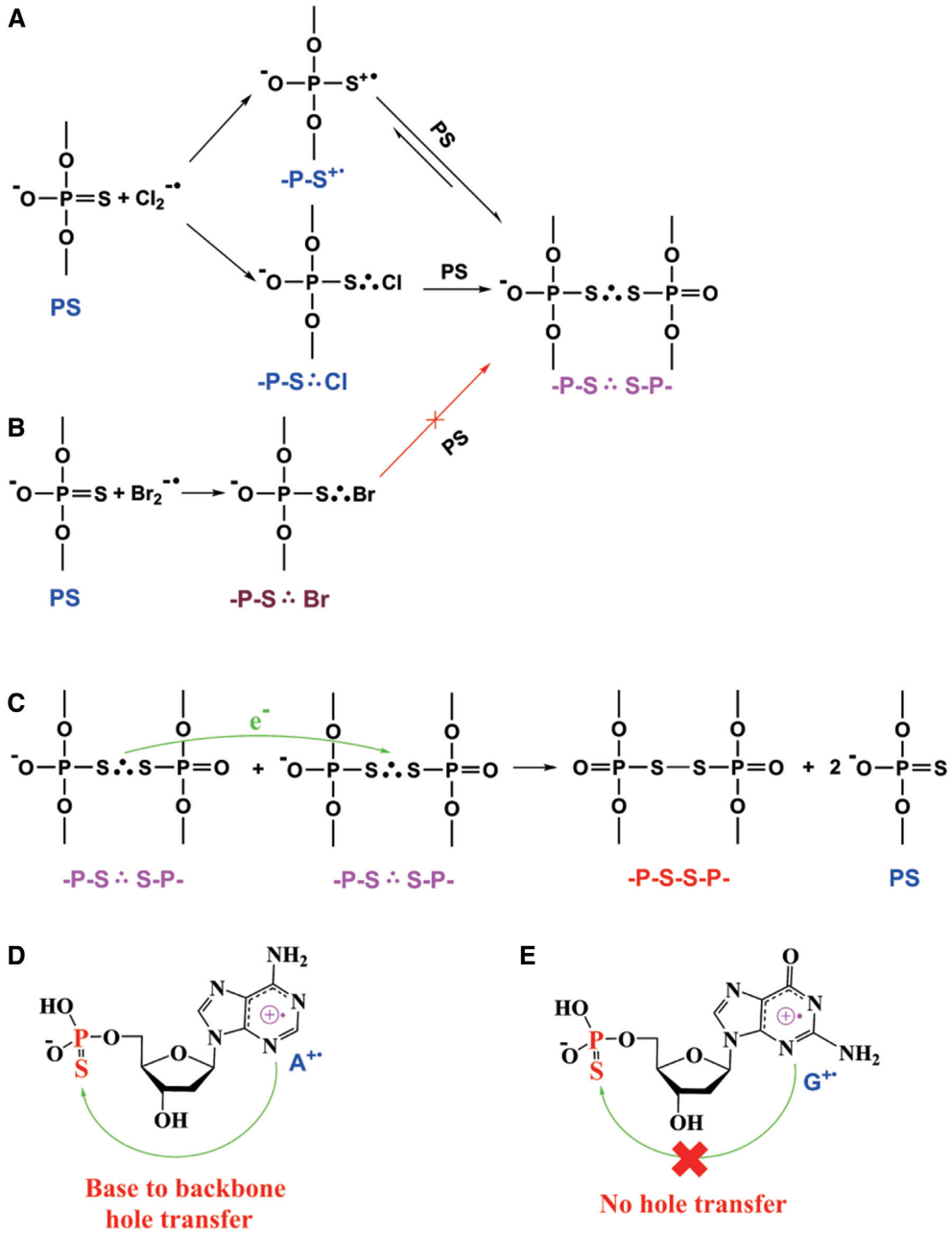


**Figure 3.** Schematic elementary oxidation mechanisms of PS in free model (*O*,*O*-diethyl thiophosphate) and PS in oligomers (*O*,*O*-dinucleoside thiophosphate) by (**A**) $Cl_2^{-\bullet}$ (strong oxidant radical) and (**B**) $Br_2^{-\bullet}$ (mild oxidant radical). (**C**) Proposed reaction scheme for the end-product -P–S–S–P- formation via the radical–radical recombination of -P–S.·.S–P-. Possible hole transfer processes (**D**) from $A^{+\bullet}$ to PS or (**E**) from $G^{+\bullet}$ to PS.

3A). While the second step is much faster, there is no concentration accumulation of the oxidation intermediates -P–S.·.Cl or -P–$S^{+\bullet}$ and this is probably why these intermediates were not observed in the transient spectra.

Similar laser flash photolysis experiments were performed for the oxidation of PS by $Br_2^{-\bullet}$. Analogous to $Cl_2^{-\bullet}$, $Br_2^{-\bullet}$ is the same kind of oxidant radical, but it is milder (52). The PS + $Br_2^{-\bullet}$ reaction should proceed via a similar mechanism and result in the possible hemi-bonded intermediate -P–S.·.Br or -P–S.·.S–P-. Prominently, in the transient spectra, the decay of $Br_2^{-\bullet}$ (at 360 nm) is accompanied by the buildup of a new species (at 380 nm) (Figure 2D and F) that corresponds to the PS + $Br_2^{-\bullet}$ reaction. Note that as shown in Figure 2D, at 420 nm, the absorbance difference between the new species and $Br_2^{-\bullet}$ is greater than that at 380 nm. We thus utilized 420 nm instead of 380 nm for monitoring the formation dynamics of the new species (Figure 2F).

Clearly, the new species at 380 nm of $Br_2^{-\bullet}$ + PS was not from -P–S.·.S–P-, but rather from another intermediate involved in the $Br_2^{-\bullet}$ + PS reaction, most likely the -P–S.·.Br intermediate. However, the -P–S.·.Br does not react further to give rise to -P–S.·.S–P- (Figure 3B), as manifested by the lack of 410 nm band in the transient spectra (Figure 2D).

This result can be rationalized by the less reactivity of -P–S.·.Br than that of -P–S.·.Cl, or, by the weaker oxidizing ability of $Br_2^{-\bullet}$, which presumably does not undergo one-electron abstraction from PS and thus there is no -P–$S^{+\bullet}$ and subsequent -P–S.·.S–P- formation.

### Theoretical calculations characterizing the spectral signature of hemi-bonded species

To aid the assignment, we further performed TD-DFT calculations to characterize the structure and spectral properties of the related radical species $Br_2^{-\bullet}$, $Cl_2^{-\bullet}$, -P–S.·.Br, -P–S.·.Cl, -P–S.·.S–P- and -P–$S^{+\bullet}$. The vibrational frequencies for the optimized structures are all positive, confirming their identity as metastable species but not transition state species. On the basis of the fully optimized geometry, the spin density distributions and the vertical excited state UV-Vis spectra were further calculated and analysed.

When the lone pair orbitals of a molecule and a radical interact to form new molecular orbitals, the bonding σ orbital is doubly occupied, while the antibonding $\sigma^*$ orbital is singly occupied (Figure 4A). The bond order of this interaction is 1/2, and such a bond is called a two-center three-electron bond (hemi-bond) (34,56,57). For the species of not only the transient intermediates (-P–S.·.Cl, -P–S.·.Br and -P–S.·.S–P-) but also the oxidant radicals ($Br_2^{-\bullet}$ and $Cl_2^{-\bullet}$), the molecular orbitals (MOs) calculated here demonstrate that the bonding σ orbital is doubly occupied, while the antibonding $\sigma^*$ orbital is singly occupied, and the spin density further shows that the unpaired spin is localized at the antibonding $\sigma^*$ orbitals on the two center atoms (Supplementary Figures S4–S8). These data characterize the hemi-bonded nature of these species.

The main MOs involved in the $\sigma \rightarrow \sigma^*$ transition overlap strongly in space (Supplementary Figures S4–S8). This enables a characteristic strong transition in the UV–vis wavelength. Among these species, the predicted strong transitions of $Cl_2^{-\bullet}$, $Br_2^{-\bullet}$, -P–S.·.Br and -P–S.·.S–P- ($\sigma\sigma^*$, Figure 4B–E) coincide generally with the intense absorption bands observed in the transient spectra (Figure 2 and Table 1), corroborating the spectral assignment of these species. In addition, the calculated absorption peak of -P–$S^{+\bullet}$ is at 321 nm ($\pi\pi^*$) with a weaker oscillator strength (0.031), which is evidently different from that observed in our transient spectra (Table 1). Therefore, the possibility of -P–$S^{+\bullet}$ as the source of the strong absorption peaks (410 or 380 nm) was ruled out. Our calculations also show that there are no strong and characteristic IR or Raman bands for -P–S.·.Br and -P–S.·.S–P-, which makes vibrational spectroscopy not feasible for the detection of these species. Fortunately, -P–S.·.Br and -P–S.·.S–P-display strong transitions in the electronic spectra and allow us to track and characterize these species through time-resolved UV–vis spectra here.

### Formation of the phosphorothioate disulfide-linked -P–S–S–P- adducts

To gain a deeper understanding of the decay fate of the hemi-bonded intermediates (-P–S.·.S–P-), we further employed high-performance liquid chromatography coupled to electrospray ionization quadrupole time-of-flight mass spectrometry (HPLC–ESI-Q-TOF-MS) to analyze the end products of the PS oxidation. Specifically, the sample solutions containing $Na_2S_2O_8$ + PS were irradiated by defined numbers (3000) of laser pulses, which triggers the formation of $SO_4^{-\bullet}$ radicals and the subsequent reaction with PS. Through HPLC analysis, three peaks with retention times of 1.29, 1.89 and 6.20 min were observed (Figure 5A). Using ESI-MS, the fractions at 1.29 min ($m/z = 193$) and 1.89 min ($m/z = 169$) were identified as the reactants $S_2O_8^{2-}$ and PS, respectively, while the fraction at 6.20 min ($m/z = 281$) was assigned to a new product species (Figure 5A), most likely the phosphorothioate disulfide adduct, -P–S–S–P- (Supplementary Figure S9) according to its mass. This fraction at 6.20 min ($m/z = 281$) does not appear without irradiation, indicating it arises from the reaction of $SO_4^{-\bullet}$ + PS.

To further identify the structure of $m/z$ 281, ESI-MS/MS was measured and the dissociation of the species of $m/z$ 281 mainly leads to the fragment ions of $m/z$ 137, $m/z$ 141, $m/z$ 169, $m/z$ 172, $m/z$ 173 and $m/z$ 201 (Figure 5B). The structures of these fragments are shown in Supplementary Figure S9. The tandem mass spectrum further supported the identification of the new product species ($m/z$ 281) as the phosphorothioate disulfide adduct, -P–S–S–P-, which is presumably originated from the decay of the intermediate -P–S.·.S–P-.

Our control experiments show that the decay kinetics of the 410 nm band for -P–S.·.S–P- is irrelevant to the presence of $O_2$ or not (Supplementary Figure S2). This indicates that -P–S.·.S–P- does not react with $O_2$ by one electron reduction to give rise to -P–S–S–P-. Calculations of AEA (adiabatic electron affinity) and reduction potentials predicted that -P–S.·.S–P- does not undergo electron-transfer reaction with $O_2$ (16). In fact, the signal of -P–S.·.S–P- sustains until ms (Figure 6), suggesting that this radical is quite stable and may have chances to undergo self-recombination. Presumably, the radical-radical recombination of two -P–S.·.S–P- by electron disproportionation could result in the formation of the end product -P–S–S–P-, and the proposed reaction scheme is illustrated by Figure 3C.

$$\frac{d[A]}{dt} = -k_1^*[A] - 2k_2^*[A]^2 \quad (5)$$

$$[A] = \frac{[A]_0^* e^{-k_1 t}}{1 + \frac{[A]_0^*(2k_2)^*(1-e^{-k_1 t})}{k_1}} \quad (6)$$

$$\Delta OD = \varepsilon^* d^* [A] \quad (7)$$

$$\Delta OD(t) = \frac{\Delta OD_0^* e^{-k_1 t}}{1 + \frac{\Delta OD_0^*(2k_2)^*(1-e^{-k_1 t})}{\varepsilon^* d^* k_1}} \quad (8)$$

Moreover, kinetics analysis shows that the decay of -P–S.·.S–P- at 410 nm cannot be described by a first-order or second-order reaction model alone, but can be well fitted with a combination model of second-order (self-recombination) and first-order reaction (Equations 5, 6, 7 and 8). Here, [A] denotes the concentration of -P–S.·.S–P-, $k_1$ is the first-order decay rate constant, $k_2$ is the second-order self-recombination rate constant, ε is extinction coef-

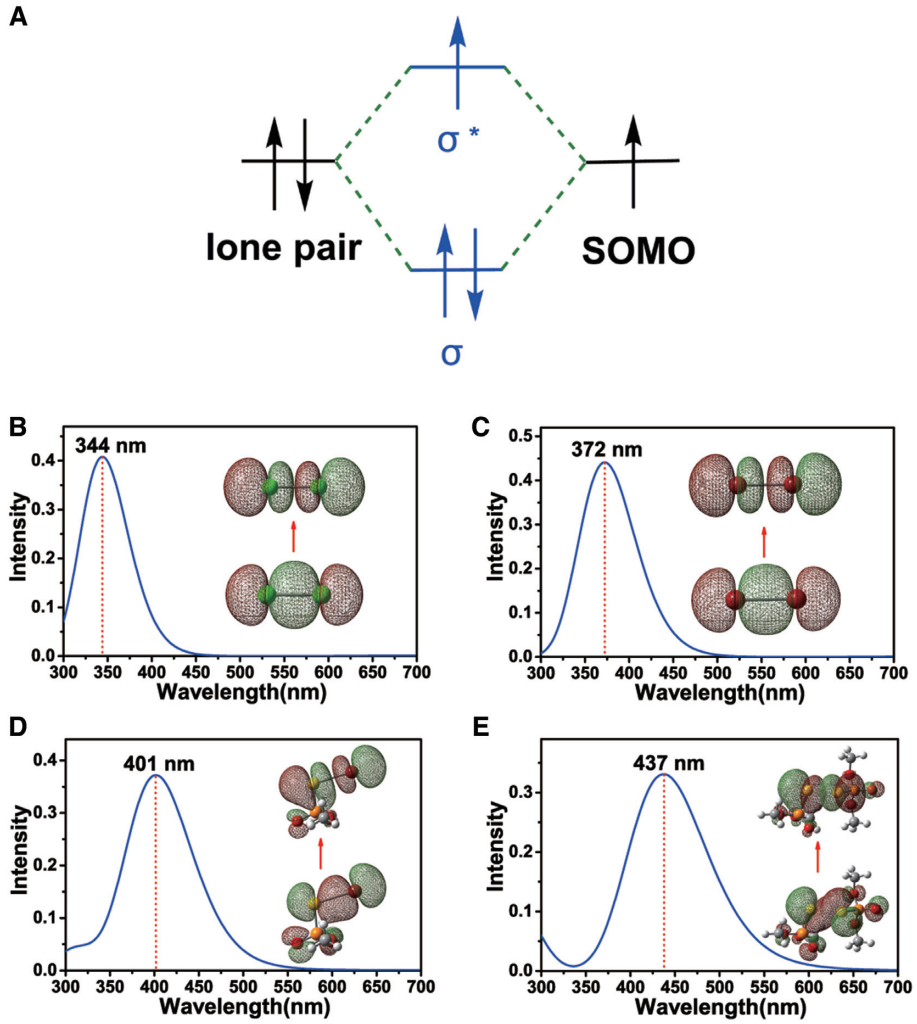


**Figure 4.** (**A**) Simplified MO energy levels for the hemi-bonded species. Calculated absorption spectra of (**B**) $Cl_2^{-\bullet}$, (**C**) $Br_2^{-\bullet}$, (**D**) -P–S.·.Br and (**E**) -P–S.·.S–P-. MOs dominantly contributing to the optical transition are also shown. Chlorine, bromine, carbon, oxygen, sulfur, phosphorus and hydrogen atoms are denoted with green, vermeil, gray, red, yellow, orange and white spheres, respectively.

**Table 1.** Optical transition data for $Cl_2^{-\bullet}$, $Br_2^{-\bullet}$, -P–S.·.Cl, -P–S.·.Br, -P–S.·.S–P- and -P–$S^{+\bullet}$. There is a general red-shift for the calculated peak wavelength λ compared to the experimental values due to the usual underestimation for the energy of excited states by TD-DFT calculation. But for the absorption maxima difference between the radicals, experimental values agree with calculations, indicating the reliability of the calculations

| | $\lambda_{exp}$ (nm) | $\lambda_{cal}$ (nm) | Oscillator strength | Transition MOs |
|---|---|---|---|---|
| $Cl_2^{-\bullet}$ | 340 | 344 | 0.408 | $\sigma \rightarrow \sigma^*$ |
| $Br_2^{-\bullet}$ | 360 | 372 | 0.441 | $\sigma \rightarrow \sigma^*$ |
| -P–S.·.Cl | – | 374 | 0.322 | $\sigma \rightarrow \sigma^*$ |
| -P–S.·.Br | 380 | 401 | 0.372 | $\sigma \rightarrow \sigma^*$ |
| -P–S.·.S–P- | 410 | 437 | 0.331 | $\sigma \rightarrow \sigma^*$ |
| -P–$S^{+\bullet}$ | – | 321 | 0.031 | $\pi \rightarrow \pi^*$ |

The main MOs involved in the $\sigma \rightarrow \sigma^*$ transition overlap strongly in space (Supplementary Figures S4–S8).

ficient of -P–S.·.S–P- at 410 nm and *d* is the optical length. Integration of Equation (5) gives Equation (6), together with Beer–Lambert Law (Equation 7), two-parameters ($k_1$, $k_2/\varepsilon d$) expression (Equation 8) is obtained and used to fit the experimental data. From the fitting, $k_1$ and $k_2/\varepsilon d$ can be obtained (Figure 6). To determine $k_2$, the extinction coefficient ε of -P–S.·.S–P- should be known.

In the consecutive radical generation processes, in principle, almost all the $SO_4^{-\bullet}$ radicals are subject to conversion to -P–S.·.S–P-. Divided by the known extinction coefficient for $SO_4^{-\bullet}$ at 450 nm (1600 $M^{-1}$ $cm^{-1}$) (48), the amount of radical can be estimated, on the basis of which the extinction coefficient of -P–S.·.S–P- at 410 nm is obtained ($\varepsilon$ = 8510 $M^{-1}$ $cm^{-1}$). Then, with this ε and the optical length *d*

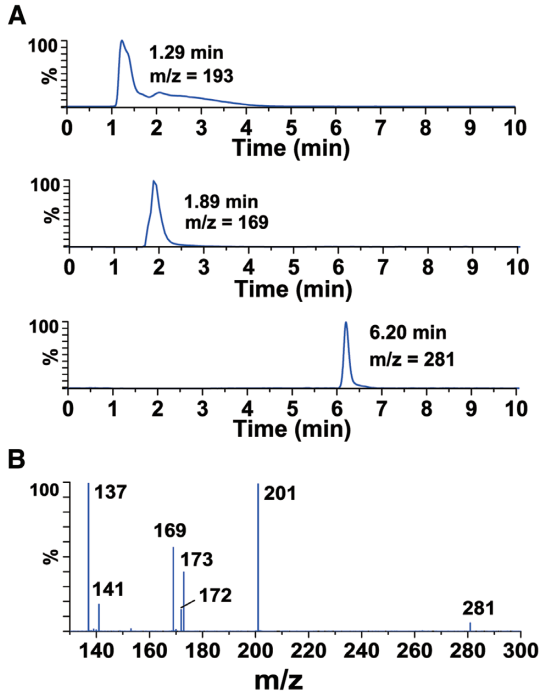


**Figure 5** Identification of the -P–S–S–P- adduct by HPLC–ESI-Q-TOF-MS analyses. The reaction solution was injected into an HPLC instrument and eluted with deionized water-acetonitrile (80:20). (**A**) Extracted ion chromatography (EIC) $m/z$ 193 at 1.29 min ($S_2O_8^{2-}$), $m/z$ 169 at 1.89 min (PS), and $m/z$ 281 at 6.20 min (oxidation products of PS). (Relative Intensity for Y-axis). (**B**) The ESI-(–)-Q-TOF-MS/MS spectrum of the $m/z$ at 281.

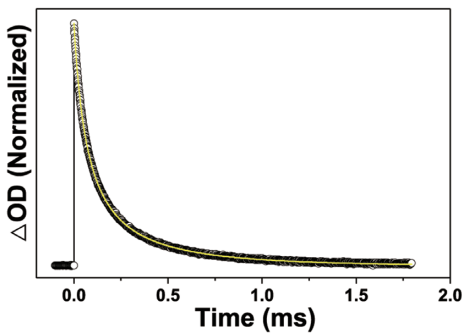


**Figure 6** Kinetics decay curve (black) for the 410 nm band of -P–S.⁻.S–P- obtained after laser flash photolysis of $Na_2S_2O_8$ + PS. Solid yellow line is the fit with a combination model of second-order and first-order reaction.

(1 cm), $k_2$ can be obtained from the fitting based on Equation (8). The second-order self-recombination rate constant $k_2$ is $5.1 \times 10^7$ $M^{-1}$ $s^{-1}$. The kinetics data here further indicate that the decay of -P–S.⁻.S–P- should involve two pathways (Figure 3): (i) the second-order self-recombination pathway via electron disproportionation, resulting in the formation of the end product -P–S–S–P- + PS; (ii) the first-order reaction pathway, presumably due to the dissociation of -P–S.⁻.S–P- to -P–$S^{+\bullet}$ + PS. The determined rate constant $k_1$ is $1.9 \times 10^3$ $s^{-1}$.

According to the HPLC–MS results and the kinetics data analysis above, the subsequent reaction of -P–S.⁻.S–P- via electron disproportionation would result in the formation of the -P–S–S–P- adduct. Given that the -P–S–S–P- adduct has a substantial bond strength (calculated to be 50.0 kcal/mol at the level of B3LYP/6–31++G(d) in the gas phase (16) and 51.6 kcal/mol here at CAM-B3LYP/6–311++G(3df,3pd) level under bulk solvation PCM model, Supplementary Figure S10), once the oxidation adduct is formed via the decay of the hemi-bonded intermediate -P–S.⁻.S–P- in the DNA backbone, it presents impediment to DNA replication or transcription. Under oxidative stress conditions, there is presence of reactive oxygen species ($H_2O_2$, $OH^\bullet$ etc). The reaction of $OH^\bullet$ with PS can induce the -P–S.⁻.S–P- radical formation (Supplementary Figure S3) and then -P–S–S–P-. Therefore, the current experiments reveal a competing pathway with the desulfurization process of PS by hydroxyl radical observed under the negative electrospray ionization mass spectroscopy conditions (58). Although it was proposed that $OH^\bullet$ underwent inelastic collisions with the negatively charged PS moiety in the atmospheric pressure ionization source to cause the S-O replacement via a PS-$OH^\bullet$ adduct, comprehensive theoretical calculations by Karwowski *et al.* (59) indicated another possibility, that is, under the negative MS collection mode, attachment of a low energy electron to the PS moiety can be an initial step leading to the cleavage of the P–S bond and then the desulfurization process. Since there is no low energy electron under physiological conditions, the oxidation of PS by $OH^\bullet$ leading to -P–S–S–P- should be a plausible pathway. It shows here that the interesting protective role of PS as an oxidation sacrifice, however, involves alternative -P–S.⁻.S–P- intermediate pathways. We also tried to study the end products and the decay pathways of the hemi-bonded intermediates (-P–S.⁻.Br). However, high salt concentrations result in ion suppression, which is one type of matrix effect that prevents measurement of liquid chromatography–mass spectrometry (LC–MS) regardless of the sensitivity or selectivity of the mass analyzer used. Therefore, samples containing $Na_2S_2O_8$ + LiBr + PS are not suitable for the HPLC–ESI-Q-TOF-MS study.

### Reaction rate constants of the oxidation of PS by $Cl_2^{-\bullet}$, $Br_2^{-\bullet}$, $SO_4^{-\bullet}$ and $OH^\bullet$ radicals

To evaluate whether the PS moiety can act as a potential redox active site and compete with guanine and adenine oxidation, the reaction rate constants were determined. As shown in Figure 2G, the 340 nm of $Cl_2^{-\bullet}$ decay rate constant increases as the PS concentration increases with a linear dependence, which further indicates that the fast decay component at 340 nm is due to the bimolecular reaction of $Cl_2^{-\bullet}$ with PS. From the slope, the second-order rate constant for the $Cl_2^{-\bullet}$ + PS oxidation is obtained as $9.4 \times 10^8$ $M^{-1}$ $s^{-1}$, which is comparable to that of $Cl_2^{-\bullet}$ + G ($\sim 7.4 \times 10^8$ $M^{-1}$ $s^{-1}$) and $Cl_2^{-\bullet}$ + A ($\sim 1.3 \times 10^8$ $M^{-1}$ $s^{-1}$) (45,60). Similarly, the second-order rate constant of the oxidation of PS + $Br_2^{-\bullet}$ is measured as $8.2 \times 10^8$ $M^{-1}$ $s^{-1}$ (Figure 2H), which is larger than that of $Br_2^{-\bullet}$ + G ($4.6 \times 10^7$ $M^{-1}$ $s^{-1}$) (61) and that of $Br_2^{-\bullet}$ + A (no reaction). The second-order rate constants measured for the oxidation of PS by $SO_4^{-\bullet}$ and $OH^\bullet$ ($\geq 1.8 \times 10^9$ and $\geq 2.5 \times 10^9$ $M^{-1}$ $s^{-1}$) (Supplementary Figures S1 and S3) are as fast as the diffusion control rate constant ($10^9$–$10^{10}$ $M^{-1}$ $s^{-1}$).

Given that both G and A are the most easily oxidized sites (61–64) in DNA and that they are the primary targets of oxidant radicals, the kinetics data obtained here indicate that the PS moiety in S-DNA can serve as an additional redox active site and may compete with the oxidation processes of G and A, thus necessitating a reevaluation of the chemical effects of the oligomer when the PS moiety is introduced.

### Monitoring oxidation of the PS moiety in competition with guanine or adenine in S-DNA oligomers

To determine the competitiveness of PS oxidation, we further investigated the oxidation of S-DNA oligomers containing both PS and G (or A) bases by highly potent radicals. Figure 7 displays the transient spectra measured for the oxidation of dinucleotide *d*[AA], *d*[$A_{PS}$A], *d*[GG] and *d*[$G_{PS}$G] by $SO_4^{-\bullet}$. The transient spectra measured for *d*[AA] and *d*[$A_{PS}$A] in Figure 7A and B, respectively, were first compared and analyzed.

For *d*[AA] + $SO_4^{-\bullet}$, the spectra display a transient feature with broad absorption bands at 330 and 590 nm. This is the characteristic absorption pattern for the one-electron oxidation product $A^{+\bullet}$ and its deprotonated neutral form A(-H)•, which is resulted from the one-electron oxidation of A by $SO_4^{-\bullet}$ and its following rapid deprotonation (loss of the amino proton) ($2.0 \times 10^7$ $s^{-1}$) (64,65). Interestingly, when PS moiety is introduced to the dinucleotide, for the *d*[$A_{PS}$A] reacting with $SO_4^{-\bullet}$, the transient spectra reveal a much more complex pattern (Figure 7B). Initially, in addition to the 330 nm band of $A^{+\bullet}$/A(-H)• (64,65), a prominent absorption band at 410 nm is also observed, which should be ascribed to -P–S.·.S–P-. Our calculations confirm that the nucleoside moiety does not influence the absorption spectrum and spin density distributions for the -P–S.·.S–P- radical in the dinucleotide (Supplementary Figure S11 and Supplementary Table S1).

According to the kinetics data above, the second-order rate constant of the $SO_4^{-\bullet}$ + PS reaction ($\geq 1.8 \times 10^9$ $M^{-1}$ $s^{-1}$) is comparable to that of the $SO_4^{-\bullet}$ + A reaction ($3.2 \times 10^9$ $M^{-1}$ $s^{-1}$) (62). Thus, at a concentration of A that is even twice as much as that of PS, the $SO_4^{-\bullet}$ + PS reaction still can compete effectively, leading to the initial formation of -P–S.·.S–P-. Besides, according to its increasing kinetics at 410 nm, the formation of the feature product -P–S.·.S–P- is characterized by two kinetics components. The rise of the fast component is at ns time scale and should be ascribed to the direct oxidation of PS by $SO_4^{-\bullet}$ based on the second-order rate constants of $SO_4^{-\bullet}$ + PS. Importantly, the slow component of -P–S.·.S–P- formation is found to be concomitant with the 330 nm decay of $A^{+\bullet}$/A(-H)•, in a rate of ∼ 2.7 μs (Figure 7B and E). This demonstrates clearly that hole transfer occurs from $A^{+\bullet}$/A(-H)• to PS as schematically shown in Figure 3D, leading to PS radical cation (-P–$S^{+\bullet}$) that is followed by the -P–S.·.S–P- formation. Thus, the hole transfer from $A^{+\bullet}$/A(-H)• to PS results in a slower formation of -P–S.·.S–P-. In this case, the fact was established that the one-electron oxidation potential for A should be higher than that for the PS moiety in the S-DNA oligomer.

However, when G with the lower oxidation potential is present in the S-DNA oligomers, for *d*[GG] and *d*[$G_{PS}$G], the transient features of both spectra are essentially the same, showing the characteristic absorption bands for $G^{+\bullet}$ and its deprotonated neutral form G(-H)• at 310, 390 and 510 nm (Figure 7C and D) (43–45,63,66), resulted from the one-electron oxidation of G by $SO_4^{-\bullet}$ and subsequent rapid deprotonation. So for *d*[$G_{PS}$G], the oxidation of PS cannot compete with that of G, and there is no hole transfer process from $G^{+\bullet}$/G(-H)• to PS as schematically shown in Figure 3E, thus there is no formation of -P–S.·.S–P-. This indicates that the one-electron oxidation potential for G is lower than that for PS, which makes the G oxidation dominant over PS in the S-oligomer and similar spectral features are observed for *d*[GG] and *d*[$G_{PS}$G]. Further, we also performed laser flash photolysis experiments for *d*[$G_{PS}$A] and *d*[$A_{PS}$G], and the obtained time-resolved spectra are the same as those for *d*[GG] and *d*[$G_{PS}$G] (Supplementary Figure S12), demonstrating that once G is close to the PS moiety, the one-electron oxidation of G is dominant, and PS cannot compete. This observation agrees with the theoretical work by Karwowski *et al.* (59) which predicted that the presence of sulfur nearby would not affect the charge distribution in the radical cations derived from *d*[GpxG] and *d*[GpxG]**d*[CpoC] (X = O or S), where the positive charge is always localized on G.

To demonstrate whether the hole transfer occurs through intrastrand or interstrand, we measured concentration dependence for the hole transfer rate. As shown in Figure 7F, the rate versus the *d*[$A_{PS}$A] concentration exhibits an independent relationship <3 mM, indicating that at low concentration conditions, the hole transfer between PS and $A^{+\bullet}$/A(-H)• occurs in the same S-DNA oligomer instead of between two separate S-DNA oligomers. Thus, the time-resolved spectral results here demonstrate the processes of base-to-backbone hole transfer from $A^{+\bullet}$/A(-H)• to PS moiety, which is different from the backbone-to-base hole transfer normally adopted in native DNA.

Overall, these results provide clear evidence for the occurrence of hole transfer from $A^{+\bullet}$/A(-H)• to PS, but not with $G^{+\bullet}$/G(-H)•. These results indicate that the redox potential of PS is higher than that of G but lower than A, which delineates the redox potential of PS between 1.29 (62,67) and 1.42 V (62,64,68) for G and A. This is a relatively small range and gives an estimation of the redox potential for PS as 1.35 ± 0.07 V. Thus, when introduced for stabilizing oligomer therapeutic agents, the PS moiety would succeed A but not G as the redox active site. PS oxidation cannot compete with G oxidation if there is G base adjacent to PS. If A is adjacent, the formation of -P–S.·.S–P- and then -P–S–S–P- can cause a type of backbone DNA lesion. Thus, the introduction of PS can play protective roles against one-electron oxidation of A. As shown in our results for *d*[$A_{PS}$A], hole transfer occurs from $A^{+\bullet}$ to PS, resulting in the repair of the A base. Thus, the redox property of PS displayed here can provide strategy for repairing oxidative base damage.

Further, the distance dependence of the hole transfer rate constants from $A^{+\bullet}$/A(-H)• to PS moiety was investigated. We performed experiments using double-stranded (ds1 and ds2) and single-stranded (ss1 and ss2) S-DNA oligomers, and the measured rate constants are listed in Table 2 and shown in Supplementary Figure S13. As expected, the hole transfer rate constants were found to de-

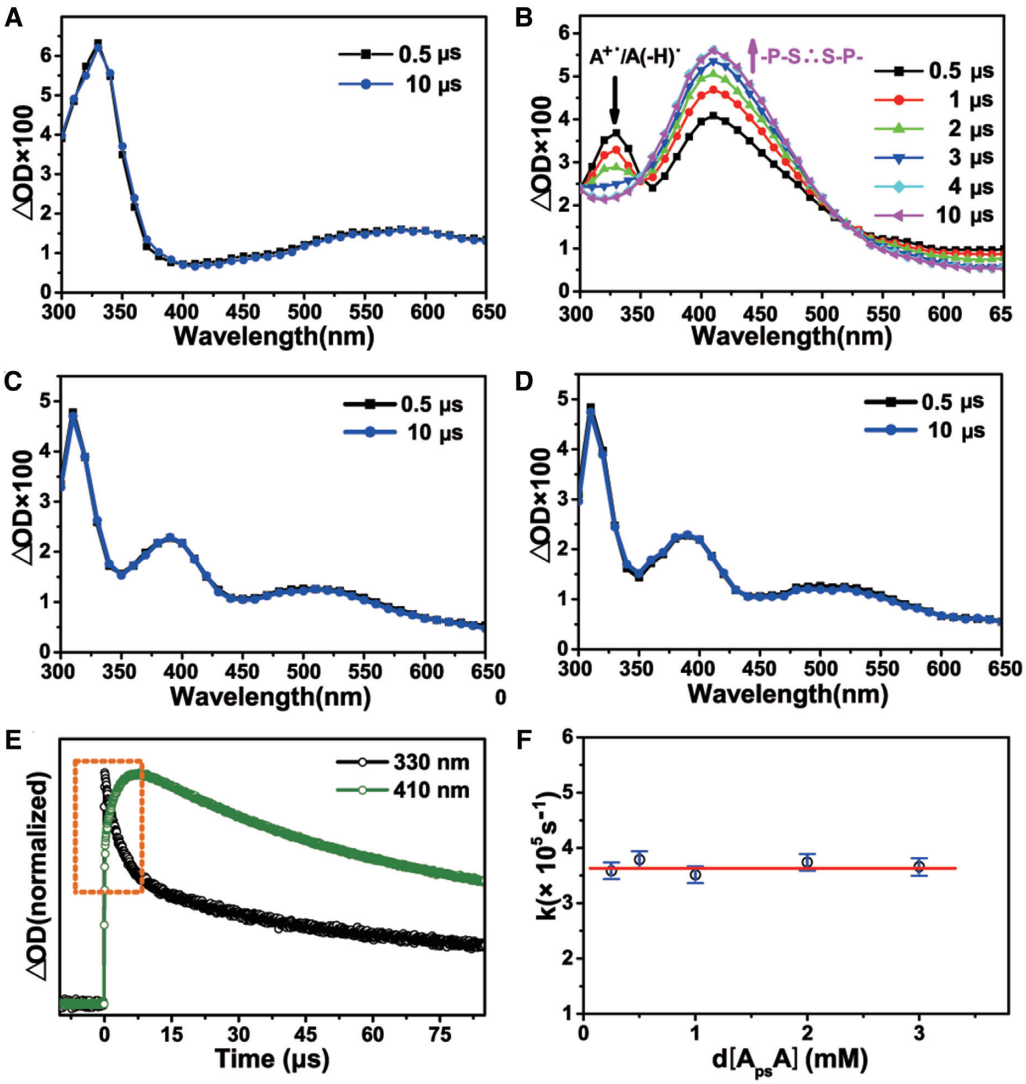


**Figure 7** Transient absorption spectra obtained after 355 nm laser flash photolysis of (**A**) $Na_2S_2O_8$ + *d*[AA], (**B**) $Na_2S_2O_8$ + *d*[$A_{PS}$A], (**C**) $Na_2S_2O_8$ + *d*[GG], and (**D**) $Na_2S_2O_8$ + *d*[$G_{PS}$G]. (**E**) Normalized absorption changes at 330 and 410 nm after laser flash photolysis of $Na_2S_2O_8$ + *d*[$A_{PS}$A]. The concentration of $Na_2S_2O_8$, *d*[GG], *d*[$G_{PS}$G], *d*[AA] and *d*[$A_{PS}$A] used in above experiments is 300, 2, 2, 2 and 2 mM, respectively. (**F**) Concentration dependence of rate constants obtained from the decay of the 330 nm bands of of $A^{+\bullet}$/A(-H).

crease with the increasing distance between A and PS moiety. In addition, the rate constants for single-stranded oligonucleotides are several folds larger than that of double-stranded oligonucleotides, and the distance dependence in double-stranded oligonucleotides is more obvious than that in single-stranded oligonucleotides. This indicates that the nature of backbone-to-base hole transfer differentiates from the base-to-base hole transfer. As is known, the latter process relies largely on the well base-stacked structure, which should be favorable for dsDNA. Whereas for the former process of backbone-to-base hole transfer, there is no stacking interaction between A and PS moiety, so the flexibility of the oligomer structure becomes more important, which is the case for single-stranded oligonucleotides. For guiding realistic application, these results suggest that when the PS is introduced into the oligonucleotides, the base-to-backbone hole transfer can be finely tuned by varying the structure and the distance between A and PS moiety in oligonucleotides, which is an intriguing process for healing the oxidized base and can be potentially exploited for the development of programmable DNA-based nanoelectronics.

**Table 2.** Sequences of the S-DNA oligomers examined in this work and the measured base-to-backbone hole transfer rate constants. PS indicates the phophorus-sulfur bond, showing where PS is incorporated

| Name | Sequence (5′to 3′) | $k$ ($s^{-1}$) |
|---|---|---|
| ds1 | 5′-$A_{ps}$ATTA$_{ps}$ATTA$_{ps}$ATT-3′<br>3′-TTA$_{ps}$ATTA$_{ps}$ATTA$_{ps}$A-5′ | $(0.8 \pm 0.1) \times 10^4$ |
| ds2 | 5′-AAT$_{ps}$TAAT$_{ps}$TAAT$_{ps}$T-3′<br>3′-T$_{ps}$TAAT$_{ps}$TAAT$_{ps}$TAA-5′ | $(0.4 \pm 0.1) \times 10^4$ |
| ss1 | 5′-$A_{ps}$ATCA$_{ps}$ATCA$_{ps}$ATC-3′ | $(3.1 \pm 0.3) \times 10^4$ |
| ss2 | 5′-AAT$_{ps}$CAAT$_{ps}$CAAT$_{ps}$C-3′ | $(2.0 \pm 0.2) \times 10^4$ |

For S-DNA, the different chiral configuration of the phosphorus atom plays a significant role for enzyme ac-

tivities. It has been known that S-oligomers in the Sp configuration is not hydrolyzed by 5′-End exonucleases opposite with that in Rp configuration (69,70). However, there is hardly any stereochemistry effect expected for the reaction studied in the current work. Basically, the hemi-bond radical intermediate formation, either -P–S.˙.X (X = Cl or Br) or -P–S.˙.S–P-, both arises from intermolecular reactions, as shown in Figure 3. This is the case not only in PS free model, but also in dinucleotide (with only one PS linker) or short oligomer (with separated PS linker), where the -P–S.˙.X is produced via bimolecular reaction of PS with $X_2^{-\bullet}$ and then -P–S.˙.X reacts with a second PS in another dinucleotide or oligomer to form -P–S.˙.S–P-. For these intermolecular reactions, the different configuration of R*p* or S*p* in phosphorothioates could have hardly any effect. Especially for the sulfur-centered hemi-bonded intermediates we are focusing on, their three-electron radical nature won't be affected by the different chiral configuration. This should be similar to the case for the radical cations derived from *d*[GpxG] and *d*[GpxG]**d*[CpoC] (X = O or S), where there is no influence of the phosphorus chirality on charge distributions (59).

## DISCUSSION

In summary, by combining time-resolved UV–vis spectroscopy and TD-DFT calculations, we have examined the elementary reaction mechanisms and dynamics of the PS oxidation by potent radicals ($Cl_2^{-\bullet}$, $SO_4^{-\bullet}$, $OH^\bullet$ and $Br_2^{-\bullet}$). The crucial sulfur-centered hemi-bonded intermediates, -P–S.˙.S–P- and -P–S.˙.Br, were observed and identified. The unique spectral signatures with a large oscillator strength ($\sigma\sigma^*$) associated with these hemi-bonded intermediates were rationalized. Kinetics analysis and HPLC-MS measurements further present evidence that the decay of -P–S.˙.S–P- can result in the formation of -P–S–S–P- adducts, which are DNA backbone lesion products. Interestingly, the oxidation rate constants of the PS moiety were found to be comparable to that of the oxidation of G and A, indicating that the PS moiety can serve as a competitive redox active site. Moreover, the oxidation of the PS moiety in dinucleotides *d*[$G_{PS}$G], *d*[$A_{PS}$A], *d*[$G_{PS}$A], *d*[$A_{PS}$G] and in S-oligomers was monitored in real-time, showing that PS oxidation can compete with adenine but not with guanine due to the subtle redox potential of PS in between G and A. Significantly, hole transfer process from $A^{+\bullet}$ to PS and concomitant -P–S.˙.S–P- formation was observed, demonstrating the base-to-backbone hole transfer unique to S-DNA, which is different from the normally adopted backbone-to-base hole transfer in native DNA. These findings reveal the distinct backbone lesion pathway brought by the PS modification, thus necessitating a re-evaluation of the chemical effects when the PS moiety is introduced for stabilizing oligonucleotide therapeutic agents, and also imply an alternative -P–S.˙.S–P-/-P–S–S–P- pathway accounting for the interesting protective role of PS as an oxidation sacrifice in bacterial genome.

## SUPPLEMENTARY DATA

Supplementary Data are available at NAR Online.

## FUNDING

National Natural Science Foundation of China [21425313, 21933005, 21773257, 21777180, 21836005] and "From 0 to 1" Original Innovation Project, the Basic Frontier Scientific Research Program, CAS [ZDBS-LY-SLH027]. Funding for open access charge: National Natural Science Foundation of China [21425313].
*Conflict of interest statement.* None declared.

## REFERENCES

1. Srinivasan,S.K and Patrick,I. (1995) Review of in vivo pharmacokinetics and toxicology of phosphorothioate oligonucleotides. *J. Clin. Lab. Anal.*, **9**, 129–137.
2. Eckstein,F. (2000) Phosphorothioate oligodeoxynucleotides: what is their origin and what is unique about them? *Antisense Nucleic Acid Drug Dev.*, **10**, 5.
3. Wilson,C. and Keefe,A.D. (2006) Building oligonucleotide therapeutics using non-natural chemistries. *Curr. Opin. Chem. Biol.*, **10**, 607–614.
4. Tsuyoshi,Y., Moeka,N., Keisuke,N. and Satoshi,O. (2011) Antisense drug discovery and development. *Future Med. Chem.*, **3**, 339–365.
5. Jansen,B. and Zangemeister-Wittke,U. (2002) Antisense therapy for cancer—the time of truth. *Lancet Oncol.*, **3**, 672–681.
6. Agrawal,S. and Kandimalla,E.R. (2001) Antisense and/or immunostimulatory oligonucleotide therapeutics. *Curr. Cancer Drug Targets.*, **1**, 13.
7. Hau,P., Jachimczak,P. and Bogdahn,U. (2009) Treatment of malignant gliomas with TGF-β2 antisense oligonucleotides. *Expert Rev. Anticancer Ther.*, **9**, 1663–1674.
8. Boado,R.J., Tsukamoto,H. and Pardridge,W.M. (1998) Drug delivery of antisense molecules to the brain for treatment of alzheimer's disease and cerebral AIDS. *J. Pharm. Sci.*, **87**, 1308–1315.
9. Kennewell,P. (2003) Technology evaluation: ISIS-104838, OraSense. *Curr. Opin. Mol. Ther.*, **5**, 76–80.
10. Van Aerschot,A. (2006) Oligonucleotides as antivirals: dream or realistic perspective? *Antiviral Res.*, **71**, 307–316.
11. Wang,L., Chen,S., Xu,T., Taghizadeh,K., Wishnok,J.S., Zhou,X., You,D., Deng,Z. and Dedon,P.C. (2007) Phosphorothioation of DNA in bacteria by dnd genes. *Nat. Chem Biol.*, **3**, 709–710.
12. Boybek,A., Ray,T.D., Evans,M.C. and Dyson,P.J. (1998) Novel site-specific DNA modification in Streptomyces: analysis of preferred intragenic modification sites present in a 5.7 kb amplified DNA sequence. *Nucleic. Acids. Res.*, **26**, 3364–3371.
13. Wu,L., White,D.E., Ye,C., Vogt,F.G., Terfloth,G.J. and Matsuhashi,H. (2012) Desulfurization of phosphorothioate oligonucleotides via the sulfur-by-oxygen replacement induced by the hydroxyl radical during negative electrospray ionization mass spectrometry. *J. Mass Spectrom.*, **47**, 836–844.
14. Cruse,W.B.T., Salisbury,S.A., Brown,T., Cosstick,R., Eckstein,F. and Kennard,O. (1986) Chiral phosphorothioate analogues of B-DNA: The crystal structure of Rp-d¦Gp(S)CpGp(S)CpGp(S)C¦. *J. Mol. Biol.*, **192**, 891–905.
15. Ozaki,H. and McLaughlin,L.W. (1992) The estimation of distances between specific backbone-labeled sites in DNA using fluorescence resonance energy transfer. *Nucleic Acids Res.*, **20**, 5205–5214.
16. Adhikary,A., Kumar,A., Palmer,B.J., Todd,A.D. and Sevilla,M.D. (2013) Formation of S–Cl phosphorothioate adduct radicals in dsDNA S-oligomers: hole transfer to guanine vs disulfide anion radical formation. *J. Am. Chem. Soc.*, **135**, 12827–12838.
17. Shukla,L.I., Adhikary,A., Pazdro,R., Becker,D. and Sevilla,M.D. (2004) Formation of 8-oxo-7,8-dihydroguanine-radicals in γ-irradiated DNA by multiple one-electron oxidations. *Nucleic Acids Res.*, **32**, 6565–6574.
18. Cadet,J., Douki,T. and Ravanat,J.L. (2008) Oxidatively generated damage to the guanine moiety of DNA: mechanistic aspects and formation in cells. *Acc. Chem. Res.*, **41**, 1075–1083.
19. Singh,T.A., Madhava Rao,B.S. and O'Neill,P. (2010) Radical chemistry of 8-oxo-7,8-dihydro-2′-deoxyadenosine and 8-oxo-7,8-dihydro-2′-deoxyguanosine: a pulse radiolysis study. *J. Phys. Chem. B*, **114**, 16611–16617.

20. Francés-Monerris,A., Merchán,M. and Roca-Sanjuán,D. (2017) Mechanism of the OH radical addition to adenine from quantum-chemistry determinations of reaction paths and spectroscopic tracking of the intermediates. *J. Org. Chem.*, **82**, 276–288.
21. Choi,Y.J., Chang,S.J., Gibala,K.S. and Resendiz,M.J.E. (2017) 8-Oxo208;7,8-dihydroadenine and 8-Oxo-7,8-dihydroadenosine—chemistry, structure, and function in RNA and their presence in natural products and potential drug derivatives. *Chem. Eur. J.*, **23**, 6706–6716.
22. Morgan,R.S., Tatsch,C.E., Gushard,R.H., Mcadon,J.M. and Warme,P.K. (1978) Chains of alternating sulfur and π-bonded atoms in eight small proteins. *Int. J. Pept. Protein Res.*, **11**, 209–217.
23. Chen,X., Tao,Y., Li,J., Dai,H., Sun,W., Huang,X. and Wei,Z. (2012) Aromatic residues regulating electron relay ability of S-containing amino acids by formations of S.·. π multicenter three-electron bonds in proteins. *J. Phys. Chem. C*, **116**, 19682–19688.
24. Orabi,E.A. and English,A.M. (2016) Sulfur-aromatic interactions: modeling cysteine and methionine binding to tyrosinate and histidinium ions to assess their influence on protein electron transfer. *Isr. J. Chem.*, **56**, 872–885.
25. Wang,D. and Fujii,A. (2017) Spectroscopic observation of two-center three-electron bonded (hemi-bonded) structures of $(H_2S)n^+$ clusters in the gas phase. *Chem. Sci.*, **8**, 2667–2670.
26. Hattori,K., Wang,D. and Fujii,A. (2019) Influence of the microsolvation on hemibonded and protonated hydrogen sulfide: infrared spectroscopy of $[(H_2S)_n(X)^1]^+$ and $H^+(H_2S)_n(X)^1$ (n = 1 and 2, X = water, methanol, and ethanol). *Phys. Chem. Chem. Phys.*, **21**, 16055–16065.
27. Wang,D., Hattori,K. and Fujii,A. (2019) The S.·. π hemibond and its competition with the S.·. S hemibond in the simplest model system: Infrared spectroscopy of the $[benzene\text{-}(H_2S)_n]^+$(n = 1–4) radical cation clusters. *Chem. Sci.*, **10**, 7260–7268.
28. Pauling,L. (1931) The nature of the chemical bond. II. The one-electron bond and the three-electron bond. *J. Am. Chem. Soc.*, **53**, 3225–3237.
29. Gilbert,B.C., Hodgeman,D.K. and Norman,R.O. (1973) Electron spin resonance studies. Part XXXVIII. Evidence for the formation of dimeric radical-cations, $R_2S.{\cdot}S_2^{+\cdot}$, in the one-electron oxidation of sulphides. *J. Chem. Soc. Perkin Trans.*, **2**, 1748–1752.
30. Bonifačić,M. and Asmus,K.-D. (1980) Stabilization of oxidized sulphur centres by halide ions. Formation and properties of $R_2S.{\cdot}X$ radicals in aqueous solutions. *J. Chem. Soc. Perkin Trans.*, **2**, 758–762.
31. Gill,P.M.W. and Radom,L. (1988) Structures and stabilities of singly charged three-electron hemibonded systems and their hydrogen-bonded isomers. *J. Am. Chem. Soc.*, **110**, 4931–4941.
32. Asmus,K.-D. (1990) *Sulfur-Centered Reactive Intermediates in Chemistry and Biology*. Springer, pp. 18.
33. Sodupe,M., Oliva,A. and Bertran,J. (1995) Theoretical study of the ionization of the $H_2S$-$H_2S$, $PH_3$-$H_2S$, and ClH-$H_2S$ hydrogen bonded molecules. *J. Am. Chem. Soc.*, **117**, 8416–8421.
34. Harcourt,R.D. (1997) Valence bond and molecular orbital descriptions of the three-electron bond. *J. Phys. Chem. A*, **101**, 2496–2501.
35. Schöneich,C., Pogocki,D., Hug,G.L. and Bobrowski,K. (2003) Free radical reactions of methionine in peptides: mechanisms relevant to β-amyloid oxidation and Alzheimer's disease. *J. Am. Chem. Soc.*, **125**, 13700–13713.
36. Shirdhonkar,M., Maity,D., Mohan,H. and Rao,B. (2006) Oxidation of methionine methyl ester in aqueous solution: a combined pulse radiolysis and quantum chemical study. *Chem. Phys. Lett.*, **417**, 116–123.
37. Hendon,C.H., Carbery,D.R. and Walsh,A. (2014) Three-electron two-centred bonds and the stabilisation of cationic sulfur radicals. *Chem. Sci.*, **5**, 1390–1395.
38. Zhang,S., Wang,X., Sui,Y. and Wang,X. (2014) Odd-electron-bonded sulfur radical cations: x-ray structural evidence of a sulfur–sulfur three-electron σ-bond. *J. Am. Chem. Soc.*, **136**, 14666–14669.
39. Xie,M., Shen,Z., Wang,D., Fujii,A. and Lee,Y.-P. (2018) Spectral characterization of three-electron two-center (3e–2c) bonds of gaseous $CH_3S.{\cdot}$. S (H) CH3 and $(CH_3SH)^{2+}$ and enhancement of the 3e–2c bond upon protonation. *J. Phys. Chem. Lett.*, **9**, 3725–3730.
40. Dreuw,A. and Head-Gordon,M. (2005) Single-reference ab initio methods for the calculation of excited states of large molecules. *Chem. Rev.*, **105**, 4009–4037.
41. Peach,M.J.G., Sueur,C.R.L., Ruud,K., Guillaume,M. and Tozer,D.J. (2009) TDDFT diagnostic testing and functional assessment for triazene chromophores. *Phys. Chem. Chem. Phys.*, **11**, 4465–4470.
42. Frisch,M.J., Trucks,G.W., Schlegel,H.B., Scuseria,G.E., Robb,M.A., Cheeseman,J.R., Scalmani,G., Barone,V., Mennucci,B., Petersson,G.A. *et al.* (Gaussian, Inc., 2013) Gaussian 09, Revision E.01.
43. Rokhlenko,Y., Geacintov,N.E. and Shafirovich,V. (2012) lifetimes and reaction pathways of guanine radical cations and neutral guanine radicals in an oligonucleotide in aqueous solutions. *J. Am. Chem. Soc.*, **134**, 4955–4962.
44. Wu,L., Liu,K., Jie,J., Song,D. and Su,H. (2015) Direct observation of guanine radical cation deprotonation in G-Quadruplex DNA. *J. Am. Chem. Soc.*, **137**, 259–266.
45. Jie,J., Liu,K., Wu,L., Zhao,H., Song,D. and Su,H. (2017) Capturing the radical ion-pair intermediate in DNA guanine oxidation. *Sci. Adv.*, **3**, e1700171.
46. Nagarajan,V. and Fessenden,R.W. (1985) Flash photolysis of transient radicals. 1. $X^{2-}$ with X = Cl, Br, I, and SCN. *J. Phys. Chem.*, **89**, 2330–2335.
47. Neta,P., Huie,R.E. and Ross,A.B. (1988) Rate constants for reactions of inorganic radicals in aqueous solution. *J. Phys. Chem. Ref. Data.*, **17**, 1027–1284.
48. McElroy,W.J. (1990) A laser photolysis study of the reaction of sulfate(1-) with chloride and the subsequent decay of chlorine(1-) in aqueous solution. *J. Phys. Chem.*, **94**, 2435–2441.
49. Yu,X., Bao,Z. and Barker,J.R. (2004) Free radical reactions involving $Cl^{\bullet}$, $Cl_2^{-\bullet}$, and $SO_4^{-\bullet}$ in the 248 nm photolysis of aqueous solutions containing $S_2O_8^{2-}$ and $Cl^-$. *J. Phys. Chem. A*, **108**, 295–308.
50. Grodkowski,J. and Neta,P. (2002) Formation and reaction of $Br_2^{\bullet-}$ radicals in the ionic liquid methyltributylammonium bis (trifluoromethylsulfonyl) imide and in other solvents. *J. Phys. Chem. A*, **106**, 11130–11134.
51. Alexander,A.J. (2003) Photofragment angular momentum polarization from dissociation of hydrogen peroxide near 355 nm. *J. Chem. Phys.*, **118**, 6234–6243.
52. Wardman,P. (1989) Reduction potentials of one-electron couples involving free radicals in aqueous solution. *J. Phys. Chem. Ref. Data.*, **18**, 1637–1755.
53. Gilbert,B.C., Larkin,J.P. and Norman,R.O.C. (1973) Electron spin resonance studies. Part XXXVII. Oxidation of [small beta]-hydroxy-sulphides by the hydroxyl radical and structural features of sulphur-conjugated radicals. *J. Chem. Soc. Perkin Trans.*, **2**, 272–277.
54. Bonifačić,M., Möckel,H., Bahnemann,D. and Asmus,K.-D. (1975) Formation of positive ions and other primary species in the oxidation of sulphides by hydroxyl radicals. *J. Chem. Soc. Perkin Trans.*, **11**, 675–685.
55. Gilbert,B.C. and Marriott,P.R. (1980) Oxidation of thiols and disulphides with the ammoniumyl radical-cation, $^{+\cdot}NH_3$: an esr investigation. *J. Chem. Soc. Perkin Trans.*, **2**, 191–197.
56. Coulson,C.A. (1952) *Valence*. Clarendon Press Oxford.
57. Maity,D.K. (2002) Sigma bonded radical cation complexes: a theoretical study. *J. Phys. Chem. A*, **106**, 5716–5721.
58. Wu,L., White,D.E., Ye,C., Vogt,F.G., Terfloth,G.J. and Matsuhashi,H. (2012) Desulfurization of phosphorothioate oligonucleotides via the sulfur-by-oxygen replacement induced by the hydroxyl radical during negative electrospray ionization mass spectrometry. *J. Mass. Spectrom.*, **47**, 836–844.
59. Karwowski,B.T. (2015) The influence of phosphorothioate on charge migration in single and double stranded DNA: a theoretical approach. *Phys. Chem. Chem. Phys.*, **17**, 21507–21516.
60. Ward,J.F. and Kuo,I. (1968) Steady state and pulse radiolysis of aqueous chloride solutions of nucleic acid components. *Advan. Chem. Ser.*, **81**, 368–373.
61. Candeias,L.P. and Steenken,S. (1989) Structure and acid-base properties of one-electron-oxidized deoxyguanosine, guanosine, and 1-methylguanosine. *J. Am. Chem. Soc.*, **111**, 1094–1099.
62. Steenken,S. (1989) Purine bases, nucleosides, and nucleotides: aqueous solution redox chemistry and transformation reactions of

their radical cations and $e^-$ and OH adducts. *Chem. Rev.*, **89**, 503–520.
63. Kobayashi,K. and Tagawa,S. (2003) Direct observation of guanine radical cation deprotonation in duplex DNA using pulse radiolysis. *J. Am. Chem. Soc.*, **125**, 10213–10218.
64. Kobayashi,K. (2010) Evidence of formation of adenine dimer cation radical in DNA: the importance of adenine base stacking. *J. Phys. Chem. B*, **114**, 5600–5604.
65. Jie,J., Wang,C., Zhao,H., Song,D. and Su,H. (2017) Experimental and theoretical study of deprotonation of DNA adenine cation radical. *Chin. J. Chem. Phys.*, **30**, 664–670.
66. Kobayashi,K., Yamagami,R. and Tagawa,S. (2008) Effect of base sequence and deprotonation of guanine cation radical in DNA. *J. Phys. Chem. B*, **112**, 10752–10757.
67. Candeias,L.P. and Steenken,S. (1992) Ionization of purine nucleosides and nucleotides and their components by 193-nm laser photolysis in aqueous solution: model studies for oxidative damage of DNA. *J. Am. Chem. Soc.*, **114**, 699–704.
68. Scheek,R.M., Stob,S., Schleich,T., Alma,N.C.M., Hilbers,C.W. and Kaptein,R. (1981) Photo-CIDNP study of adenosine 5′-monophosphate. Pair-substitution effects due to cation radical deprotonation. *J. Am. Chem. Soc.*, **103**, 5930–5932.
69. Stec,W.J., Karwowski,B., Boczkowska,M., Guga,P., Koziołkiewicz,M., Sochacki,M., Wieczorek,M.W. and Błaszczyk,J. (1998) Deoxyribonucleoside 3‘-O-(2-thio- and 2-oxo-“spiro”-4,4-pentamethylene-1,3,2-oxathiaphospholane)s: monomers for stereocontrolled synthesis of oligo(deoxyribonucleoside phosphorothioate)s and chimeric PS/PO oligonucleotides. *J. Am. Chem. Soc.*, **120**, 7156–7167.
70. Piotr,G. (2007) P-Chiral oligonucleotides in biological recognition processes. *Curr. Top. Med. Chem.*, **7**, 695–713.